Confined Nanobubbles Shape the Surface Roughness Structures of Thin Film Composite Polyamide Desalination Membranes

Xiaoxiao Song[a,*], Bowen Gan[a], Zhe Yang[b], Chuyang Y. Tang[b,c,d*], Congjie Gao[a]

[a] Centre for Membrane Separation and Water Science & Technology, Ocean College, Zhejiang University of Technology, Hang Zhou, 310014, P. R. China

[b] Department of Civil Engineering, the University of Hong Kong, Pokfulam, Hong Kong

[c] UNESCO Centre for Membrane Science and Technology, School of Chemical Engineering, University of New South Wales, Sydney, New South Wales 2052, Australia

[d] UNSW Water Research Centre, School of Civil and Environmental Engineering, University of New South Wales, Sydney, New South Wales 2052, Australia

[*] Corresponding Author.

Xiaoxiao Song Tel: +86 (0571) 8832 4135, E-mail address: songxiaoxiao@zjut.edu.cn

Chuyang Y. Tang Tel: +852 2859 1976, Fax: +852 2559 5337, E-mail address: tangc@hku.hk

Abstract

The ridge-and-valley roughness structure of a polyamide reverse osmosis (RO) membrane has a paramount impact on its separation performance. We show that this surface roughness appearance was shaped by gas nanobubbles confined between the polyamide rejection layer and the substrate. Performing interfacial polymerization (IP) under alternative confinement conditions led to drastically different surface morphologies, e.g., smooth polyamide surface formed at support-free aqueous/organic interfaces whereas crater-like features formed in inversed IP. For the first time, we demonstrated the collapse of fully hydrated balloon-like nodules into dehydrated leaf-like and donut-like roughness features during membrane drying by performing an *in-situ* atomic force microscopic characterization. Deformation of roughness features caused by dehydration was not fully reversible, which correlates well with the dramatic reduction of membrane permeability upon drying. Our study provides a fundamental framework for the surface roughness formation in RO membranes, which is critical for advancing roughness control technologies with enhanced membrane performance.

INTRODUCTION

Thin film composite reverse osmosis (TFC-RO) membranes represent the state-of-the-art technology for desalination and water reuse [1, 2]. Their polyamide rejection layer, prepared by an interfacial polymerization (IP) reaction between an aqueous solution of aromatic amines and an organic solution of acyl chlorides [1, 3, 4], presents nanoscale heterogeneous surface [5, 6] with unique roughness features commonly known as the "ridge-and-valley" structures [7-13]. The surface roughness of TFC-RO membranes has paramount effect on their separation performance [12, 14-19]. For example, greatly improved water permeability has been correlated with increased membrane surface roughness [10, 17, 20, 21].

The formation of the roughness features in the polyamide rejection layer has been traditionally explained by the diffusion of amine monomers (e.g., m-phenylenediamine (MPD)) into the organic solution of acyl chlorides (e.g., trimesoyl chloride (TMC)) and the instability of the reaction interface [22-28]. However, these simple models could not explain the formation of smooth polyamide layers at low MPD-TMC concentrations [28, 29]. In a recent work, Ma et al. [20] revealed that nanosized gas bubbles such as CO_2, released from the aqueous amine solution due to the generation of acid and heat during the IP reaction, is responsible for the roughness formation in a polysulfone (PSF) supported polyamide layer. This nanofoaming mechanism is supported by the presence of numerous nanosized voids within the polyamide rejection layer (up to 32% by volume fraction) [7-9, 30]. It further explains the disappearance of the surface

roughness by using low MPD-TMC concentrations [28, 31], pre-degassing the amine solution before IP [20], or prolonging the reaction duration to allow better heat dissipation (e.g., by electrospray-assisted IP) [32, 33]. Nevertheless, nanofoaming alone is inadequate to explain the role of the substrate on surface roughness [34, 35], such as the formation of a smooth polyamide film at a free water/hexane interface [29]. The apparent failure of Ma's nanofoaming theory prompts us to hypothesize that the confinement of the nanobubbles plays a critical role in shaping the ridge-and-valley roughness appearance and that the removal of confinement leads to the disappearance of these characteristic features. Accordingly, we designed different IP routes to systematically create different confinement conditions and investigate their effect on roughness generation. We further hypothesize that the nanovoids-containing roughness features undergo deformation upon dehydration. In this study, for the first time, we developed an *in-situ* atomic force microscopic (AFM) method for continuous monitoring of membrane roughness during an entire drying cycle. We show that the commonly reported ridge-and-valley structures are the compounded effects of the creation of nanovoids by confined nanobubbles during IP and their subsequent partial collapse upon drying. The fine elucidation of the roughness structures and their formation mechanisms in our study provide a fundamental framework for tailoring surface roughness of TFC-RO membranes and advance the understanding of their transport behavior.

METHODOLOGY

Fabrication of membranes

All TFC-RO membranes were prepared by the IP reaction of 2% MPD aqueous solution and 0.1% TMC hexane solution. Three different IP routes were adopted to systematically investigate the confinement effect (Figure 1a). In the normal IP (n-IP), we followed a conventional method [31]: an MPD-impregnated PSF substrate (Aromem Pte. Ltd., Suzhou, China) was soaked in a TMC solution for 2 mins to form a thin polyamide layer. We also conducted an invert IP (i-IP) process by switching the sequence of MPD and TMC application. Specifically, the support membrane was first impregnated with 0.1% TMC hexane solution. To minimize the hydrolyzation of TMC, the adsorbed water in the PSF substrate was replaced first with pure ethanol, ethanol/hexane, and primed by pure hexane for 10 minutes in sequence and then soaked in 0.1% TMC/hexane solution for another 5 minutes. Figure S1 shows the solvent infiltration step did not alter the permeability of the PSF substrate. The TMC impregnated substrate was contacted with the 2% MPD aqueous solution immediately for 2 minutes to allow the IP reaction to complete. During this process, the substrate was floated on the surface of the MPD solution with a top-side-down manner due to the density difference. The f-IP reaction was carried out at a support-free interface between an MPD aqueous solution and TMC hexane solution in a glass container. For characterization, the PA layer was further loaded on an AAO membrane/silicon wafer for microscopic characterization. For performance characterization purpose, the PA

layer was loaded onto a PSF substrate by performing the f-IP reaction in the funnel of a vacuum filter assembly (KG-90, ADVANTEC, JAPAN) preloaded with a wet PSF substrate. The IP reaction (2 min) was terminated by the drainage of the MPD solution (pumped through the PSF substrate) and removing of excess TMC solution (manually, using a pipette). Finally, the vacuum was continued for ~10 minutes until the f-IP membrane is bond with the PSF substrate. The polyamide layers formed by n-IP, f-IP, and i-IP were denoted as n-PA, f-PA, and i-PA, respectively. All the membranes were washed thoroughly and preserved in DI water until further usage.

Characterization of membrane morphology

Microscopical studies for dry membranes

Surface and cross-sectional morphologies of membranes were characterized by an ultrahigh-resolution Hitachi 8010U FESEM unit. Cross-sectional images were produced by fracturing membrane coupons in liquid nitrogen. Prior to observation, the samples were sputter coated with Pt at standard coating distance (~ 8 cm) with a 15 mA current. Surface samples were coated for 30 seconds and cross-section samples were coated for 45 seconds respectively. Topological images in air and liquid were obtained using an atomic force microscope (AFM, ICON, Bruker, Billerica, MA). Unless specified, the cantilever was scanasyst-air/fluid and the work mode was tapping. Free-standing polyamide (PA) selective layers were isolated by dissolving the substrate PSF layer in pure DMF. Thorough washing of a PA layer with DMF comprises of 3 cycles of rinsing (3 minutes) and soaking (10 minutes). The neat PA layer was transparent and

no white color precipitates can be observed on its top. The free-standing polyamide layer was then transferred onto silicon wafer for further characterization or analysis.

Microscopical studies for wet membranes

An *in-situ* AFM method was developed to monitor the morphological changes of n-PA during an air-drying cycle. A nascent membrane in its wet state was sealed with O-ring in a liquid cell assembly (EC Cell Assembly, Bruker, Billerica, MA) with only its polyamide surface exposed to the ambient air (26 °C, 40% RH) to allow the evaporation of water while performing AFM measurements (TESPA-V2 cantilever, tapping mode, 1 Hz scan rate). Upon the disappearance of the excess water layer on the membrane surface, AFM images were taken approximately every 13 minutes according to the scan settings, and the drying was continued for 65 minutes.

Separation performance tests

Membrane separation performance (flux and salt rejection) was tested with a lab-scale cross-flow RO test setup. The diameter of the circular-shaped membrane cell was 5 cm and the feed channel depth was 2.5 mm. The cross-flow velocity and pressure were 1.6 L/min and 2.0 MPa, respectively. All membranes were compacted with DI water for 1 hour, then the flux and NaCl (2000 ppm) rejection were tested over a duration of 1 hour. The A and B values were calculated following in accordance to our previous publication [31].

Membrane rehydration

Membrane samples were first dried in a fumehood (25 °C, 70% RH for 2 hrs) or in an

oven (80 °C for 30 mins). In a comparative study, a membrane coupon was soaked with 10% glycerol/water for 60 minutes and then dried in the fumehood. Rehydration was performed by soaking n-PA membrane samples in deionized (DI) water, 0.1% sodium dodecyl sulphate (SDS) solution, or 80% ethanol. For *ex-situ* AFM characterization, rehydration of the oven-dried sample was performed with the following treatments in sequence: soaking in DI water for 36.5 hours, prewetting with 50/50 (v/v) IPA/water and then soaking in DI water for another 6 hours, followed by a further forward osmosis (FO) treatment using 4 M NaCl as draw solution on the rejection layer side and DI water on the PSF substrate side. The FO treatment was designed to utilize the FO water flux to restore the polyamide nodules. Briefly, a wet membrane was clamped between two solution compartments and sealed with silicone rubber sheet. The solution compartment facing the membrane top surface was filled with 4M NaCl, and the other compartment facing the support side was filled with DI water. Water was continuously drawn from the support side chamber to the draw solution side. The duration of the FO treatment was 1 hour. It is worthwhile to note that the FO treatment was adopted as a means to investigate the reversibility of nodule deformation. This treatment is not recommended for implementation for large plants due to the potential risk of delamination of the PA layer from its substrate.

RESULTS AND DISCUSSION

Confined nanobubbles mold the surface roughness of TFC-RO membranes

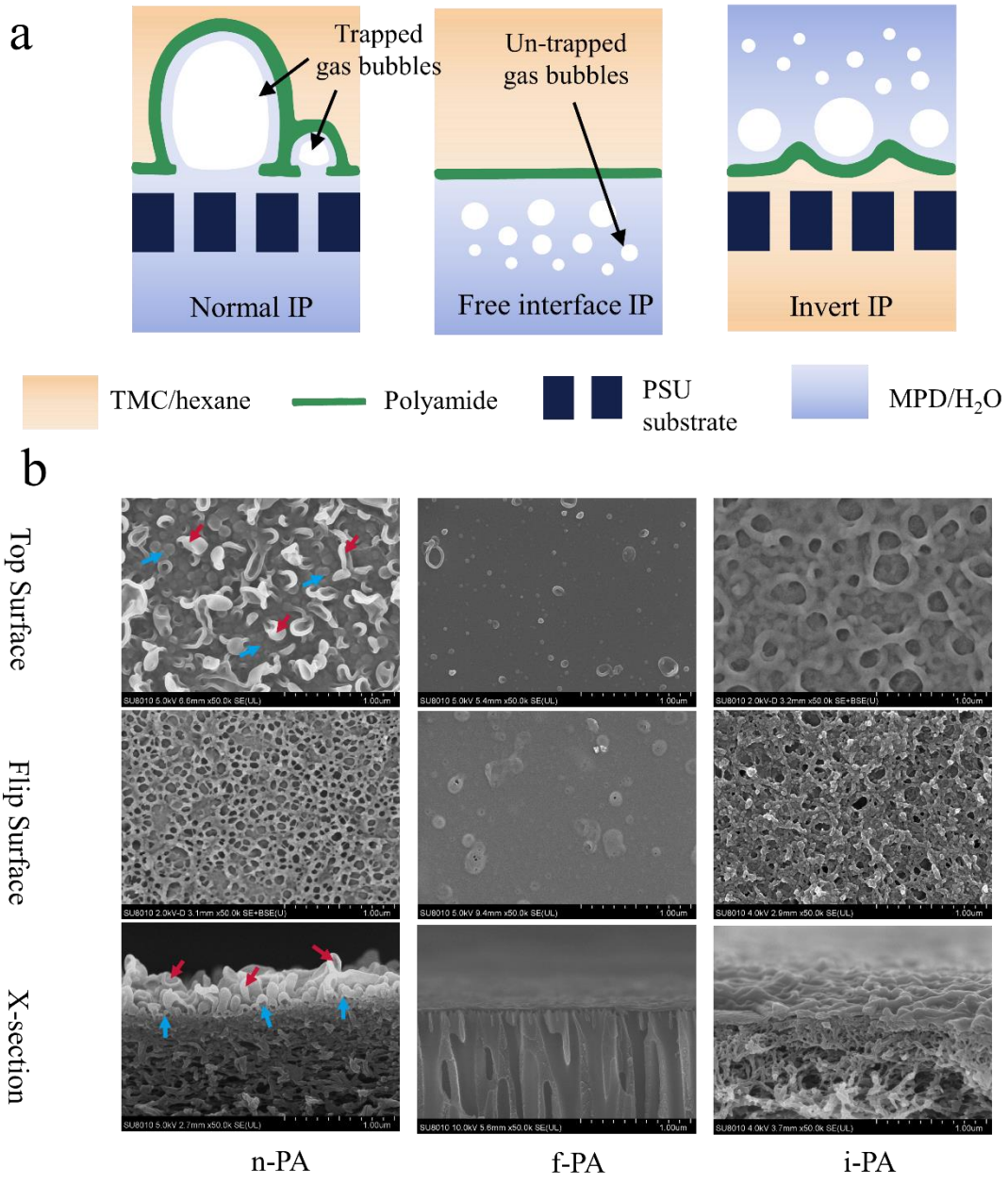

Figure 1. (a) The formation of PA layer during n-IP, f-IP, and i-IP. n-IP: normal interfacial polymerization method using PSF support membrane. f-IP: free interface interfacial polymerization. i-IP: invert interfacial polymerization method (TMC soaking followed by MPD soaking) using PSF support membrane. (b) FESEM morphological characterization for n-PA, f-PA, and i-PA membranes: top surfaces (upper panel), flip surfaces (middle panel) and cross sections (lower panel). The polyamide layers formed by n-IP, f-IP, and i-IP methods were denoted as n-PA, f-PA,

and i-PA, respectively.

The top surface of the n-PA was characterized by a "ridge-and-valley" appearance showing both small globular nodules and some elongated "leaf-like" structures (shown by blue and red arrows in Figure 1b, respectively), in good agreement with the literature [4, 5, 11, 12, 14, 36-39]. Its average surface roughness (R_a) was 54.2 nm (Figure 2a), which is typical for polyamide desalination membranes [31, 40]. The cross-sectional view (Figure 1b) shows densely-packed nodules standing side-by-side at the base of the selective layer, together with leaf-like features extending to the upper part of the selective layer. The cross-section also shows the presence of nanovoids inside these roughness features [6-8, 11, 26, 27, 41], which extended all the way to the flip side of the n-PA layer (Figure 3). Consequently, its flip side exhibits a honeycomb-like structure. The morphology of this honeycomb-like structure remained unchanged with prolonged soaking in DMF (Figure S2), implying that these structural features were not artifacts resulting from the DMF treatment. The formation of hollow nodules and leaves can be explained by the degassing of CO_2 nanobubbles from the amine solution with the release of heat and acid during the IP reaction (Figure 1a) [20]. Due to the significant resistance to air movement by the PSF substrate, i.e., the confinement effect, the degassed nanobubbles tend to grow towards the reaction interface where a polyamide film is rapidly formed [31]. Therefore, the "ridge-and-valley" appearance is a result of molding polyamide by the trapped nanobubbles. Upon the formation of a gas-tight polyamide film at the reaction interface, any further release of gas now has to escape

from its flip-side, which interrupts the complete encapsulation of the nanovoids to form the honeycomb-like pores to facilitate air passages.

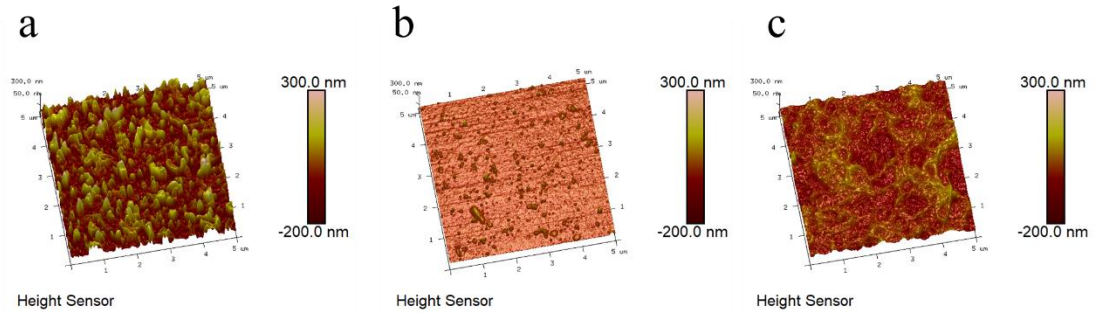

Figure 2. The 3D representation AFM micrographs of (a) n-PA, (b) f-PA, and, (c) i-PA surfaces. Their average surface roughness (R_a) were 54.2, 4.1, and 23.0 nm, respectively. The color scale for the data has been unified to facilitate comparison.

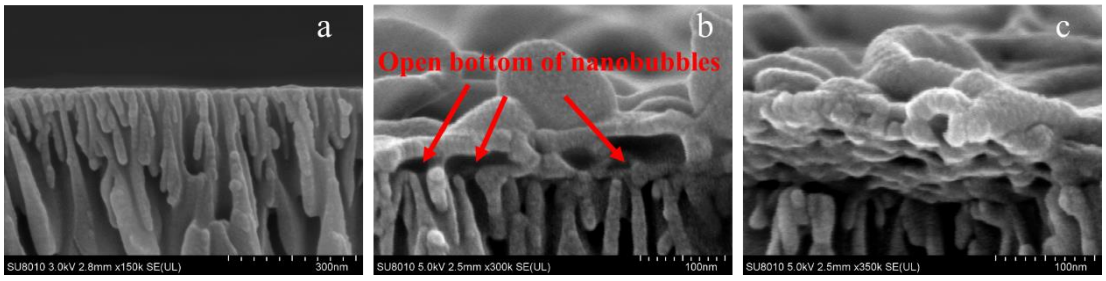

Figure 3. The FESEM image of (a) the cross-section of the bare AAO substrate and (b) the cross-section of a n-PA layer transferred onto the AAO substrate, and (c) a tilted section that showing the bottom side of the n-PA layer. The SEM images present clearly visible nanovoids within the polyamide roughness features. These nanovoids are connected to the honeycomb-like pores in the flip-side of n-PA.

To further test the role of confinement, f-IP and i-IP were performed under otherwise identical reaction conditions. The resultant f-PA had a much smoother surface (R_a = 4.1 nm, see Figure 2b). FESEM micrographs (Figure 1b) reveals that this membrane was nearly free of the conventional roughness features. In contrast, the i-PA layer exhibits a "crater-like" structure with moderate roughness (R_a = 23.0 nm, see Figure 2c). These

apparently disparate results are the direct consequence of the different confinement conditions. During i-IP, CO_2 nanobubbles released from the aqueous side of the reaction interface. Unlike the case of n-IP where the nanobubbles are sandwiched between the polyamide film and the substrate, gas bubbles produced in i-IP are expected to have lower pressure due to the lack of confinement from the aqueous solution side. This lower pressure allows the formation of larger bubbles. The bubbles push monomer solutions to their surroundings, yet these movements are constrained laterally by the PSF support. Therefore, the growth of the larger bubbles together with the constraints by the PSF support molds the cater-like features, with some craters as large as ~ 0.5 μm in diameter (Figure 1a and Figure S3). For the case of f-IP at a support-free interface, the total lack of constraint by a substrate (allowing the polyamide film to be smoothen out more easily) and the presence of a large reservoir of high-pH amine solution at ~ pH 9.7 (allowing bubbles to be more readily dissolved) result in the formation of a smooth PA layer.

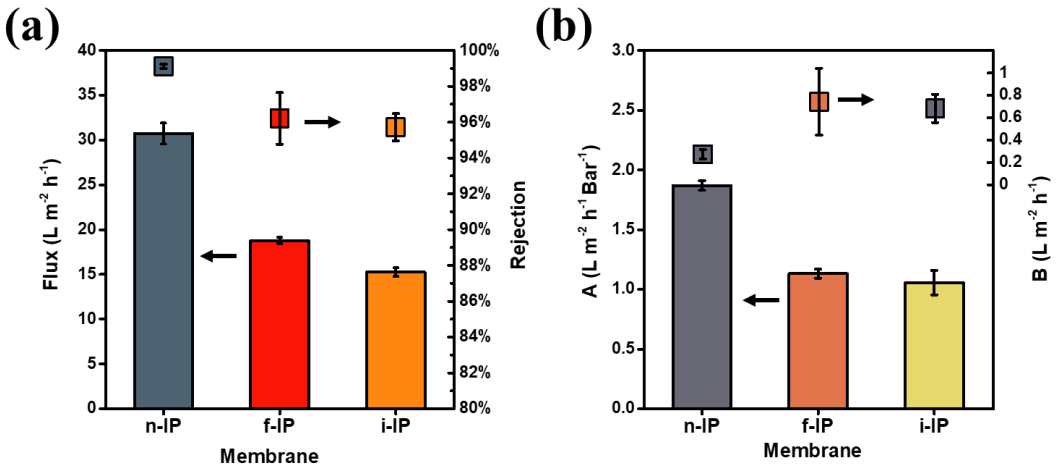

Figure 4. The (a) flux/rejection and (b) A/B value of the n-IP, f-IP, and i-IP membranes. All membranes were tested using a feed solution of 2000 ppm NaCl at an applied pressure of 2.0 MPa. Data reported was based on the average of 3 membrane samples for n-IP and i-IP or 5 membrane samples for f-IP. The greater number of samples was adopted for f-IP due to the slightly greater variation for its rejection data (refer to Table S1).

Compared to n-PA, the water permeability of f-PA and i-PA was nearly halved (Figure 4) with the absence of ostentatious nodules/leaves (i.e., reduced surface area), which provide direct evidence that the presence of these roughness features enhances membrane permeability. On the other hand, the NaCl rejection of f-PA and i-PA was also greatly reduced (and the *B* value was increased), which may be caused by defects generated in their fabrication processes. For example, nano-sized pinholes were observed on top of the i-PA membrane (Figure S3). In contrast, the better rejection of n-PA can be potentially explained by a "spontaneous self-healing" mechanism. The presence of moderately pressurized nanobubbles in the confined space forces the aqueous amide solution to the defect sites (if any), whose interfacial polymerization

with TMC will then seal these defects. Nevertheless, excessive formation of nanobubbles could disrupt the formation of an intact polyamide film. The results in the current study conclude the critical importance of nanobubble confinement on shaping the roughness of TFC-RO membranes and determining their separation performance.

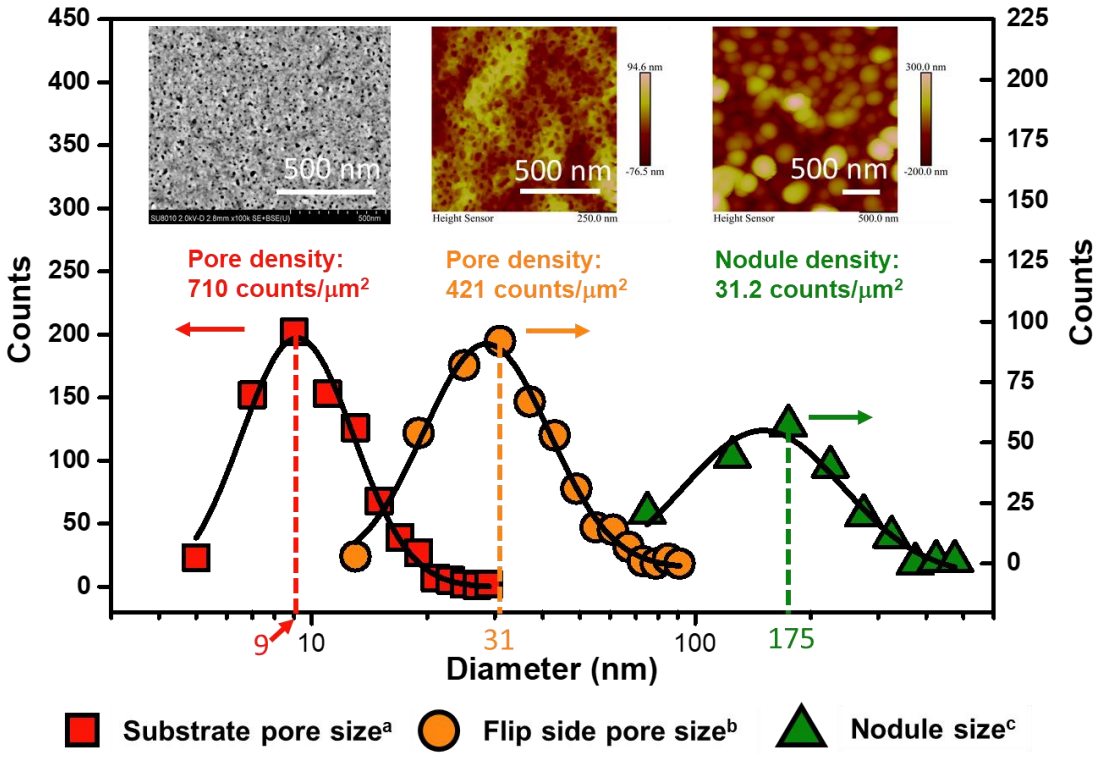

Figure 5. Size distribution of surface roughness features of the n-PA layer, honeycomb-like pores on its flip-side, and pores of the PSF substrate. The representative micrographs (from left to right) show a typical FESEM/AFM micrograph of the PSF, the n-PA flip surface, and the n-PA top surface. AFM was performed for a well hydrated n-PA layer (see details in Figure 7). Note: sizes are reported based on all structures counted on a certain scanned area (a: PSF substrate pores, ~1.14 μm^2, 807 pores; b: PA flipside, 1.0 μm^2, 421 openings; c: PA surface layer, 6.25 μm^2, 195 nodules). Please refer to Figure S4 for the detailed information regarding analysis of the structural features.

We further analyzed the size distribution and number density for the roughness features of the n-PA membrane, in relation to its substrate pores and the honeycomb-like pores

observed from the flip-side of the polyamide layer (Figure 5). The nodules of the n-PA surface had a number density of 31.2 counts/μm^2, and its size distribution followed a log-normal pattern with the highest frequency of size centering at ~ 175 nm. In contrast, significantly more pores were observed (421 counts/μm^2) with much smaller size (centered at ~ 31 nm) on its flip side. These results suggest that each nanovoid within a roughness nodule may be connected to multiple pores on the flip side of the polyamide layer. Analysis of the PSF substrate reveals even smaller pore size (centered at ~ 9 nm) with higher number density (710 counts/μm^2), suggesting that the pores at PA flip side may span over multiple pores on the PSF substrate to result in an overall number ratio of 1 nodule to 13 flip side pores and 23 substrate pores. Our results are consistent to a previous study reporting that each roughness feature corresponds to multiple pores in the substrate [42]. While this hierarchic nanocavity-pore connectivity is formed during the IP reaction to facilitate the degassing through the substrate, such a structure ensures an unobstructed pathway to water transport as well.

Dehydration causes partial collapse of roughness features

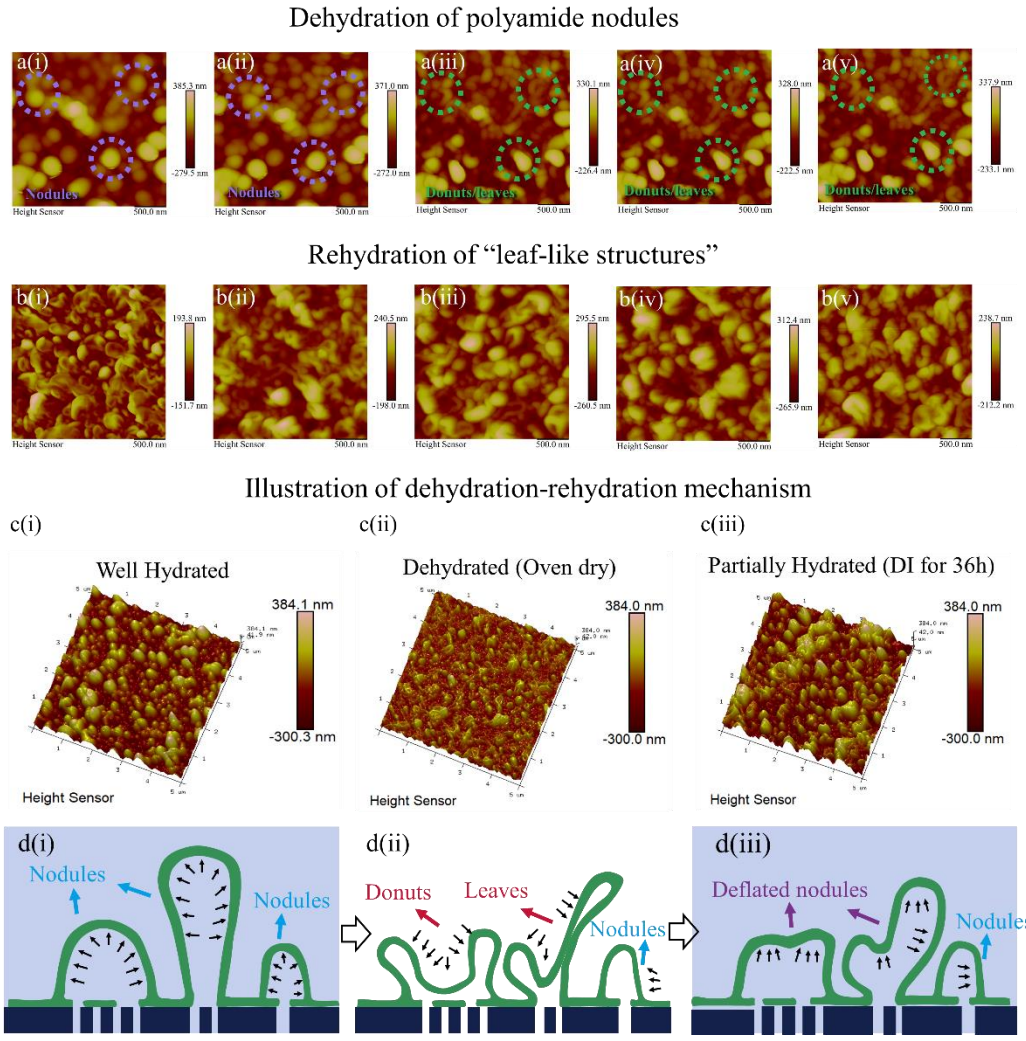

Figure 6. Dehydration and rehydration of n-PA. **(**a) *In-situ* AFM observation of dehydration of the n-PA membrane (top surface) over a 65-minute duration. All images (i-v) were scanned bottom up, with scanning time of about 13 minutes (which was required for an image to be accomplished according to the scan settings). During the dehydration process, some large size nodules (blue dotted circles) transformed into donut/leaf-like structures (green dotted circles). (b) *Ex-situ* AFM observation of the impact of rehydration conditions on the n-PA morphology. All images were taken for the same sample after the following treatments in sequence: (i) drying in oven at 80 °C for 30 mins; (ii) rehydration in DI water for 30 minutes; (iii) rehydration in DI water for another 36 hours; (iv) an additional treatment by prewetting with 50/50 (v/v) IPA/water and then rehydration in DI water for another 6 hours; (v) a further forward osmosis (FO) treatment. (c) The 3D AFM micrographs of (i) the well-hydrated n-PA surface, (ii) dehydrated n-PA surface in 80 °C oven for 30 minutes, and (iii) partially rehydrated n-PA surface in DI water (same rehydration condition with b(iii)). (d)

289 Schematics of deformation of polyamide roughness features during dehydration and
290 rehydration.

291

292 Since surface roughness of n-PA is shaped by nanobubbles, one would expect "balloon-
293 like" (rounded or ellipsoidal) nodules. However, the n-PA top surface (Figure 1)
294 presents features mostly resembling deflated balloons. This difference can be possibly
295 reconciled considering the effect of sample drying. We therefore performed an *in-situ*
296 AFM scan of a nascent n-PA membrane in its fully hydrated conditions and its
297 subsequent time-dependent morphological changes upon drying (Figure 6). The fully
298 hydrated n-PA (Figures 6a(i) and 6c(i)) shows a distinctive morphology characterized
299 by balloon-like features (i.e., fully inflated nodules) of variable sizes, which supports
300 the nanofoaming theory. Upon air drying over a period of 65 minutes (Figure 6a(i-v)),
301 some balloons slowly became deflated, which can be attributed to the capillary forces
302 during drying. In particular, the larger balloons (~ or > 300 nm in size) were transformed
303 into flattened leaf-like structures, and some smaller balloons collapsed into "donut-like"
304 shapes. We further performed *ex-situ* drying of the n-PA membrane in oven (Figure
305 6b(i)), which led to even more severe collapse of balloons. Our *in-situ* and *ex-situ* AFM
306 observations provide direct evidence, for the first time, that the ridge-and-valley
307 structure observed in dry state is the compounded result of nanofoaming and drying and
308 that the leaf-like structures originate from the collapse of large nodules upon
309 dehydration.

310

Conversely, the collapsed roughness features can be partially restored by rehydration in DI water for a certain period (Figure 6b(ii, iii)). Rehydration using IPA (Figure 6(iv)), a commonly used wetting agent, appeared to be more effective than DI water in the restoration of the features. Nevertheless, IPA rehydration (Figure 6(iv)) and the use of osmotic flow (Figure 6b(v)) could not restore the nodules into their fully inflated states, suggesting that the deformation was partially irreversible.

Dehydration compromises membrane permeability

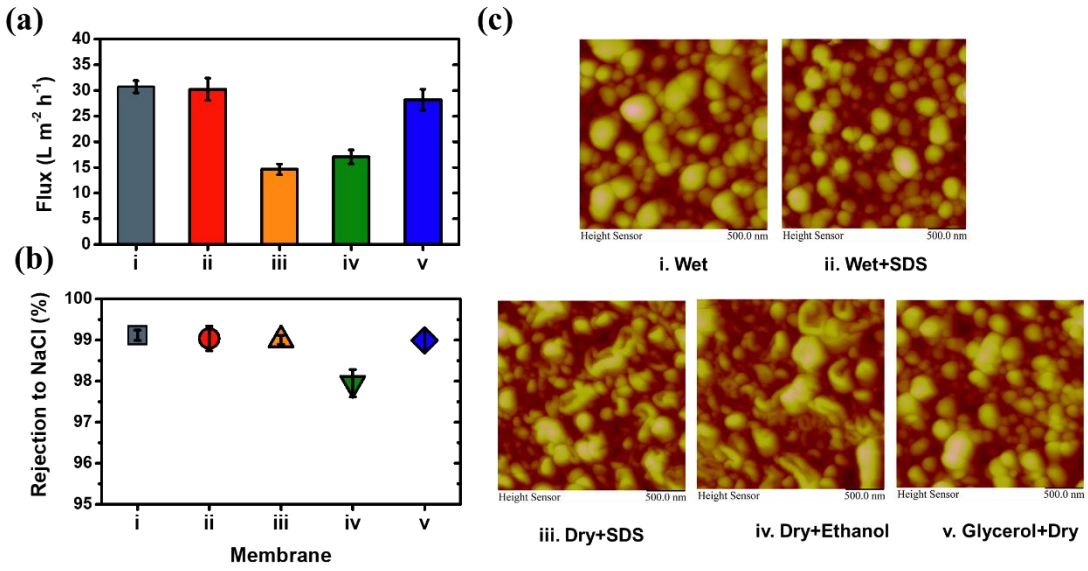

Figure 7. The comparison of membrane performance under various wetting/rehydration conditions (from condition i to v): (a) flux, and (b) NaCl rejection of the said membranes. (c) The morphology of the said membranes characterized by AFM. All membranes are tested using a feed solution was 2000 ppm NaCl at an applied pressure of 2.0 MPa. Data is reported based on the average of 3 membrane samples.

The membrane permeability was found to be greatly affected by its hydration status. The flux of the fully hydrated membrane (Figure 7, membrane i) was 30.7 ± 1.2 L m^{-2}

h^{-1}. The presence of SDS in the wetting solution (Figure 7, membrane ii) had little effect on the membrane flux. After ambient drying in a fumehood (25 °C and 70% RH), the membrane lost nearly half of its permeability regardless if 0.1% SDS (Figure 7, membrane iii) or 80% ethanol (Figure 7, membrane iv) was used for the rehydration. Although these wetting agents are known to provide good rehydration for the PSF substrates [43-45], they were unable to fully recover the rounded structure of the nodules. Therefore, the reduced membrane permeability can be attributed to the partial collapse of balloon-like nodules. This effect is consistent with the greater transport resistance to water within the reduced volume of the nanovoids [46]. Conversely, if the nodular structures were preserved (e.g., by pre-soaking the membrane with 10% glycerol before drying), the flux was not significantly deteriorated (Figure 7, membrane v). The strong correlation between the membrane permeability and the hydrated PA morphology reveals that proper preservation techniques are essential to maintain the high performance of TFC-RO membranes. With the exception of ethanol treatment, the salt rejection was well maintained during dehydration/rehydration. The treatment with ethanol, however, resulted in significantly lower NaCl rejection, possibly due to its ability to swell the polyamide network [47-50]. This study reveals the ability of glycerol for maintaining the PA morphology and separation performance during drying process, which echoes with the industrial practice of using preservation fluid during membrane delivery and storage [51].

IMPLICATIONS AND PERSPECTIVES

Our study elucidates for the first time the role of nanobubble confinement on the polyamide morphology. The pristine balloon-like morphology of the nascent polyamide layer was revealed, which sets a milestone on the understanding of the formation and transport mechanisms of the PA layer. We provide compelling evidence on the collapse of these balloon-like features upon dehydration, which is accompanied with dramatic reduction of separation performance. Since most literature studies perform surface morphological characterization and separation performance tests using membranes with a drying history, our study suggests a critical need for the membrane community to systematically address the issue of membrane drying and preservation.

Our study also sets a fundamental framework for understanding the formation of PA layer. Although polyamide is believed to formed in the organic solution side of the IP reaction interface [3], future studies should also systematically investigate the aqueous side behaviors during the IP reaction. For example, the “volcanic eruption” model [34] has been often used to explain the effect of the substrate pores. Such nanoscale volcanic eruptions, if exist, might be related to the generation of gas bubbles within the substrate pores. The fact that each nanocavity within the polyamide layer is connected to multiple pores in the substrate may further suggest concerted volcanic eruptions from multiple pores, instead of isolated eruptions from each individual pore that is often implicitly assumed.

The current study reveals a strong dependence membrane separation performance on the roughness features. The n-PA has much greater water permeability compared to i-PA and f-PA thanks to the formation of the balloon-like roughness features that provide increased filtration area. Therefore, fine engineering of the roughness structures [17] and nanofoaming of the PA layer [20, 52] may provide rational solutions to the development of high performance membranes. Future studies are also needed to further investigate the role of nanobubbles and the associated roughness structures on the rejection and selectivity of TFC polyamide membranes [52].

ACKNOWLEDGMENTS

This research was funded by the National Key R&D Program of China (No. 2017YFC0403903) and the National Natural Science Foundation of China (No. 21706231). We are thankful for Aromem Pte. Ltd. (Suzhou, China) for providing free PSF substrate samples. Special thanks are given to Dr. Liu Yang (Bruker, Beijing office) for his helpful discussions in wet state AFM analysis and Dr. Jiang Zhiwei (Imperial College, London) for his suggestions on the fabrication of f-IP membrane.

REFERENCE

[1] M. Elimelech, W.A. Phillip, The Future of Seawater Desalination: Energy, Technology, and the Environment, Science, 333 (2011) 712.

[2] C.Y. Tang, Z. Yang, H. Guo, J.J. Wen, L.D. Nghiem, E. Cornelissen, Potable Water Reuse through Advanced Membrane Technology, Environmental Science & Technology, 52 (2018) 10215-10223.

393 [3] J.E. Cadotte, Evolution of Composite Reverse Osmosis Membranes, in: Materials
394 Science of Synthetic Membranes, American Chemical Society, 1985, pp. 273-294.
395 [4] R.J. Petersen, Composite reverse osmosis and nanofiltration membranes, J. Membr.
396 Sci., 83 (1993) 81-150.
397 [5] V. Freger, Nanoscale Heterogeneity of Polyamide Membranes Formed by Interfacial
398 Polymerization, Langmuir, 19 (2003) 4791-4797.
399 [6] M.M. Kłosowski, C.M. McGilvery, Y. Li, P. Abellan, Q. Ramasse, J.T. Cabral, A.G.
400 Livingston, A.E. Porter, Micro-to nano-scale characterisation of polyamide structures
401 of the SW30HR RO membrane using advanced electron microscopy and stain tracers,
402 J. Membr. Sci., 520 (2016) 465-476.
403 [7] M. Kurihara, M. Hanakawa, Mega-ton Water System: Japanese national research
404 and development project on seawater desalination and wastewater reclamation,
405 Desalination, 308 (2013) 131-137.
406 [8] H. Yan, X. Miao, J. Xu, G. Pan, Y. Zhang, Y. Shi, M. Guo, Y. Liu, The porous
407 structure of the fully-aromatic polyamide film in reverse osmosis membranes, J. Membr.
408 Sci., 475 (2015) 504-510.
409 [9] L. Lin, R. Lopez, G.Z. Ramon, O. Coronell, Investigating the void structure of the
410 polyamide active layers of thin-film composite membranes, J. Membr. Sci., 497 (2016)
411 365-376.
412 [10] C. Kong, M. Kanezashi, T. Yamomoto, T. Shintani, T. Tsuru, Controlled synthesis
413 of high performance polyamide membrane with thin dense layer for water desalination,
414 J. Membr. Sci., 362 (2010) 76-80.
415 [11] F.A. Pacheco, Microscopic characterization of the nanostructure of polyamide thin
416 films in reverse osmosis and nanofiltration membranes, Ph.D. Thesis. Standford
417 University, (December 2011).
418 [12] A.K. Ghosh, B.-H. Jeong, X. Huang, E.M.V. Hoek, Impacts of reaction and curing
419 conditions on polyamide composite reverse osmosis membrane properties, J. Membr.
420 Sci., 311 (2008) 34-45.
421 [13] F.A. Pacheco, I. Pinnau, M. Reinhard, J.O. Leckie, Characterization of isolated
422 polyamide thin films of RO and NF membranes using novel TEM techniques, J. Membr.
423 Sci., 358 (2010) 51-59.
424 [14] S.H. Kim, S.-Y. Kwak, T. Suzuki, Positron Annihilation Spectroscopic Evidence
425 to Demonstrate the Flux-Enhancement Mechanism in Morphology-Controlled Thin-
426 Film-Composite (TFC) Membrane, Environmental Science & Technology, 39 (2005)
427 1764-1770.
428 [15] M. Hirose, Y. Minamizaki, Y. Kamiyama, The relationship between polymer
429 molecular structure of RO membrane skin layers and their RO performances, J. Membr.
430 Sci., 123 (1997) 151-156.
431 [16] S. Al-Jeshi, A. Neville, An investigation into the relationship between flux and
432 roughness on RO membranes using scanning probe microscopy, Desalination, 189
433 (2006) 221-228.

[17] Z. Tan, S. Chen, X. Peng, L. Zhang, C. Gao, Polyamide membranes with nanoscale Turing structures for water purification, Science, 360 (2018) 518.
[18] X. Li, T.-S. Chung, T.-S. Chung, Effects of free volume in thin-film composite membranes on osmotic power generation, AlChE J., 59 (2013) 4749-4761.
[19] L. Shen, W.-s. Hung, J. Zuo, X. Zhang, J.-Y. Lai, Y. Wang, High-performance thin-film composite polyamide membranes developed with green ultrasound-assisted interfacial polymerization, J. Membr. Sci., 570-571 (2019) 112-119.
[20] X.-H. Ma, Z.-K. Yao, Z. Yang, H. Guo, Z.-L. Xu, C.Y. Tang, M. Elimelech, Nanofoaming of Polyamide Desalination Membranes To Tune Permeability and Selectivity, Environ. Sci. Technol. Lett., 5 (2018) 123-130.
[21] M. Hirose, H. Ito, Y. Kamiyama, Effect of skin layer surface structures on the flux behaviour of RO membranes, J. Membr. Sci., 121 (1996) 209-215.
[22] V. Freger, Kinetics of Film Formation by Interfacial Polycondensation, Langmuir, 21 (2005) 1884-1894.
[23] L.J.J.M. Janssen, K. te Nijenhuis, Encapsulation by interfacial polycondensation. I. The capsule production and a model for wall growth, J. Membr. Sci., 65 (1992) 59-68.
[24] P.W. Morgan, S.L. Kwolek, Interfacial polycondensation. II. Fundamentals of polymer formation at liquid interfaces, Journal of Polymer Science, 40 (1959) 299-327.
[25] J. Muscatello, E.A. Müller, A.A. Mostofi, A.P. Sutton, Multiscale molecular simulations of the formation and structure of polyamide membranes created by interfacial polymerization, J. Membr. Sci., 527 (2017) 180-190.
[26] H.F. Ridgway, J. Orbell, S. Gray, Molecular simulations of polyamide membrane materials used in desalination and water reuse applications: Recent developments and future prospects, J. Membr. Sci., 524 (2017) 436-448.
[27] J. Lee, A. Hill, S. Kentish, Formation of a thick aromatic polyamide membrane by interfacial polymerisation, Sep. Purif. Technol., 104 (2013) 276-283.
[28] S. Karan, Z. Jiang, A.G. Livingston, Sub-10 nm polyamide nanofilms with ultrafast solvent transport for molecular separation, Science, 348 (2015) 1347-1351.
[29] Z. Jiang, S. Karan, A.G. Livingston, Water Transport through Ultrathin Polyamide Nanofilms Used for Reverse Osmosis, Adv. Mater., 30 (2018) 1705973.
[30] J. Xu, H. Yan, Y. Zhang, G. Pan, Y. Liu, The morphology of fully-aromatic polyamide separation layer and its relationship with separation performance of TFC membranes, J. Membr. Sci., 541 (2017) 174-188.
[31] X. Song, S. Qi, C.Y. Tang, C. Gao, Ultra-thin, multi-layered polyamide membranes: Synthesis and characterization, J. Membr. Sci., 540 (2017) 10-18.
[32] X.-H. Ma, Z. Yang, Z.-K. Yao, H. Guo, Z.-L. Xu, C.Y. Tang, Interfacial Polymerization with Electrosprayed Microdroplets: Toward Controllable and Ultrathin Polyamide Membranes, Environ. Sci. Technol. Lett., 5 (2018) 117-122.
[33] M.R. Chowdhury, J. Steffes, B.D. Huey, J.R. McCutcheon, 3D printed polyamide membranes for desalination, Science, 361 (2018) 682.

475 [34] A.K. Ghosh, E.M.V. Hoek, Impacts of support membrane structure and chemistry
476 on polyamide–polysulfone interfacial composite membranes, J. Membr. Sci., 336 (2009)
477 140-148.
478 [35] M. Shi, Z. Wang, S. Zhao, J. Wang, S. Wang, A support surface pore structure re-
479 construction method to enhance the flux of TFC RO membrane, J. Membr. Sci., 541
480 (2017) 39-52.
481 [36] M. Elimelech, Z. Xiaohua, A.E. Childress, H. Seungkwan, Role of membrane
482 surface morphology in colloidal fouling of cellulose acetate and composite aromatic
483 polyamide reverse osmosis membranes, J. Membr. Sci., 127 (1997) 101-109.
484 [37] C.Y. Tang, Y.-N. Kwon, J.O. Leckie, Characterization of Humic Acid Fouled
485 Reverse Osmosis and Nanofiltration Membranes by Transmission Electron Microscopy
486 and Streaming Potential Measurements, Environmental Science & Technology, 41
487 (2007) 942-949.
488 [38] J. Yin, E.-S. Kim, J. Yang, B. Deng, Fabrication of a novel thin-film nanocomposite
489 (TFN) membrane containing MCM-41 silica nanoparticles (NPs) for water purification,
490 J. Membr. Sci., 423-424 (2012) 238-246.
491 [39] Y.-F. Mi, Q. Zhao, Y.-L. Ji, Q.-F. An, C.-J. Gao, A novel route for surface
492 zwitterionic functionalization of polyamide nanofiltration membranes with improved
493 performance, J. Membr. Sci., 490 (2015) 311-320.
494 [40] C.Y. Tang, Y.-N. Kwon, J.O. Leckie, Effect of membrane chemistry and coating
495 layer on physiochemical properties of thin film composite polyamide RO and NF
496 membranes: II. Membrane physiochemical properties and their dependence on
497 polyamide and coating layers, Desalination, 242 (2009) 168-182.
498 [41] O. Coronell, B.J. Mariñas, D.G. Cahill, Depth Heterogeneity of Fully Aromatic
499 Polyamide Active Layers in Reverse Osmosis and Nanofiltration Membranes,
500 Environmental Science & Technology, 45 (2011) 4513-4520.
501 [42] X. Lu, L.H. Arias Chavez, S. Romero-Vargas Castrillón, J. Ma, M. Elimelech,
502 Influence of Active Layer and Support Layer Surface Structures on Organic Fouling
503 Propensity of Thin-Film Composite Forward Osmosis Membranes, Environmental
504 Science & Technology, 49 (2015) 1436-1444.
505 [43] J. Kochan, T. Wintgens, R. Hochstrat, T. Melin, Impact of wetting agents on the
506 filtration performance of polymeric ultrafiltration membranes, Desalination, 241 (2009)
507 34-42.
508 [44] S. Shultz, M. Bass, R. Semiat, V. Freger, Modification of polyamide membranes
509 by hydrophobic molecular plugs for improved boron rejection, J. Membr. Sci., 546
510 (2018) 165-172.
511 [45] J.R. McCutcheon, M. Elimelech, Influence of membrane support layer
512 hydrophobicity on water flux in osmotically driven membrane processes, J. Membr.
513 Sci., 318 (2008) 458-466.
514 [46] M.C.Y. Wong, L. Lin, O. Coronell, E.M.V. Hoek, G.Z. Ramon, Impact of liquid-
515 filled voids within the active layer on transport through thin-film composite membranes,

516 J. Membr. Sci., 500 (2016) 124-135.
517 [47] V. Freger, Swelling and Morphology of the Skin Layer of Polyamide Composite
518 Membranes: An Atomic Force Microscopy Study, Environmental Science &
519 Technology, 38 (2004) 3168-3175.
520 [48] X. Qiao, T.-S. Chung, Fundamental Characteristics of Sorption, Swelling, and
521 Permeation of P84 Co-polyimide Membranes for Pervaporation Dehydration of
522 Alcohols, Industrial & Engineering Chemistry Research, 44 (2005) 8938-8943.
523 [49] J.S. Louie, I. Pinnau, M. Reinhard, Effects of surface coating process conditions
524 on the water permeation and salt rejection properties of composite polyamide reverse
525 osmosis membranes, J. Membr. Sci., 367 (2011) 249-255.
526 [50] E.P. Chan, A.P. Young, J.-H. Lee, C.M. Stafford, Swelling of Ultrathin Molecular
527 Layer-by-Layer Polyamide Water Desalination Membranes, J. Polym. Sci., Part B:
528 Polym. Phys., 51 (2013) 1647-1655.
529 [51] Dow Water & Process Solutions, FILMTEC^{TM} Reverse Osmosis Membranes
530 Technical Manual, Https://msdssearch.dow.com
531 [52] X. Ma, Z. Yang, Z. Yao, H. Guo, Z. Xu, C.Y. Tang, Tuning roughness features of
532 thin film composite polyamide membranes for simultaneously enhanced permeability,
533 selectivity and anti-fouling performance. J. Colloid Interface Sci. 540 (2019) 382-388.